ISSN 1990-7931, Russian Journal of Physical Chemistry B, 2025, Vol. 19, No. 2, pp. 480–500. © Pleiades Publishing, Ltd., 2025.

CHEMICAL PHYSICS OF NANOMATERIALS

Unraveling Hetero-Clusters of Indium Gallium Nitride and Its Alloys for Solar Cells Development: Structural and Characterization Study of Nitride-Based Semiconductors Using DFT Framework

F. Mollaamin[a], * and M. Monajjemi[b]

[a] *Department of Biomedical Engineering, Faculty of Engineering and Architecture, Kastamonu University, Kastamonu, Turkey*

[b] *Department of Chemical Engineering, Central Tehran Branch, Islamic Azad University, Tehran, Iran*

** e-mail: fmollaamin@kastamonu.edu.tr*

Received July 21, 2024; revised November 16, 2024; accepted November 20, 2024

Abstract—This work wants to investigate hetero-clusters of Ga_8N_9, In_8N_9, $In_4Ga_4N_9$, $Si-In_3Ga_4N_9$, $Zn-In_3Ga_4N_9$, $Ag-In_3Ga_4N_9$ can attract considerable attention for storage energy in solar cells. A comprehensive investigation on energy grabbing by Ga_8N_9, In_8N_9, $In_4Ga_4N_9$, $Si-In_3Ga_4N_9$, $Zn-In_3Ga_4N_9$, $Ag-In_3Ga_4N_9$ was carried out including using DFT computations at the CAM–B3LYP–D3/6-311+G(*d*, *p*) level of theory. Electromagnetic and thermodynamic properties of Ga_8N_9, In_8N_9, $In_4Ga_4N_9$, $Si-In_3Ga_4N_9$, $Zn-In_3Ga_4N_9$, $Ag-In_3Ga_4N_9$ hetero-clusters have been evaluated. The hypothesis of the energy adsorption phenomenon was confirmed by density distributions of CDD, TDOS/OPDOS and ELF for Ga_8N_9, In_8N_9, $In_4Ga_4N_9$, $Si-In_3Ga_4N_9$, $Zn-In_3Ga_4N_9$, $Ag-In_3Ga_4N_9$ hetero-clusters. The two hetero-clusters of $Zn-In_3Ga_4N_9$ and $Ag-In_3Ga_4N_9$ with the fluctuations of In, Ga, N and transition metals of Zn, Ag have indicated the same sensitivity graph of electric potential via charge distribution with $R^2_{Zn/Ag-In_4Ga_4N_9} = 0.9998$. In InGaN, the photo excited electrons and holes are strongly bounded by the excitons because of their large exciton binding energy as $E^o_{Ag-In_3Ga_4N_9} > E^o_{Zn-In_3Ga_4N_9} > E^o_{Si-In_3Ga_4N_9}$ due to its efficient exciton dissociation. Therefore, it can be considered that zinc and silver atoms in the functionalized $Zn-In_3Ga_4N_9$ and $Ag-In_3Ga_4N_9$ might have more impressive sensitivity for accepting the electrons in the process of energy adsorption mechanism. The changes of Gibbs free energy versus dipole moment could detect the maximum efficiency of $Ag-In_3Ga_4N_9$ hetero-cluster for energy storage in the solar cells through $\Delta G^o_{f,Ag-In_3Ga_4N_9} = -409.008 \times 10^3$ kcal/mol. As a matter of fact, it can be observed that doped hetero-clusters of $Zn-In_3Ga_4N_9$ and $Ag-In_3Ga_4N_9$ might ameliorate the capability of $In_4Ga_4N_9$ in solar cells for energy storage.

Keywords: hetero cluster, solar cells, energy saving, materials modeling

DOI: 10.1134/S1990793125700174

1. INTRODUCTION

A binary III/V direct bandgap semiconductor called Gallium nitride (GaN) is a very hard material with wide bandgap applied in a variety of technologies, including optoelectronic, high-power electronics and light-emitting diodes, partly due to its favorable thermal properties [1–4]. The nitrides of group III in periodic table have low sensitivity to ionizing radiation which make them appropriate materials for solar cell arrays for satellites. Therefore, space applications could also benefit as devices have shown stability in high radiation environments. Because GaN transistors can operate at much higher temperatures and work at much higher voltages than gallium arsenide (GaAs) transistors, they make ideal power amplifiers at microwave frequencies. In addition, GaN offers promising characteristics for THz devices. Due to high power density and voltage breakdown limits GaN is also emerging as a promising candidate for 5G cellular base station applications [5–8].

GaN with a high crystalline quality can be obtained by depositing a buffer layer at low temperatures [9, 10]. Such high-quality GaN led to the discovery of *p*-type GaN [11], *p–n* junction blue/UV-LEDs [5] and room-temperature stimulated emission [12]. This has led to the commercialization of high-performance blue LEDs and long-lifetime violet laser diodes, and to the development of nitride-based devices such as UV detectors and high-speed field-effect transistors [13]. GaN-based metal–oxide–semiconductor field-effect transistor (MOSFET) and metal–semiconductor field-effect transistor (MESFET) transistors also

offer advantages including lower loss in high power electronics, especially in automotive and electric car applications [14]. The U.S. Army Research Laboratory (ARL) provided the first measurement of the high field electron velocity in GaN in 1999 [15]. Scientists at ARL experimentally obtained a peak steady-state velocity of 1.9×10^7 cm/s, with a transit time of 2.5 ps, attained at an electric field of 225 kV/cm. With this information, the electron mobility was calculated, thus providing data for the design of GaN devices.

Solar cells of ternary alloys such as indium gallium nitride (InGaN) are attracting interest due to the tunable direct band gap energy of InGaN covering the whole solar spectrum ranging from 0.7 eV (band gap energy of InN) to 3.4 eV (band gap energy of GaN) [16, 17], as well as superior photovoltaic characteristics of InGaN including high absorption coefficients (~ 105 cm^{-1}) [18] and high carrier mobility. Moreover, high stability (thermal and chemical) and superior radiation resistance of InGaN alloys allow operation of InGaN-based devices in extreme conditions such as space and terrestrial applications [16, 19]. InGaN-based solar cells have been successfully fabricated with low indium contents of the InGaN alloy [20–22]. Lower indium content in InGaN leads to an increase in the band gap energy of InGaN, which in turn results in the absorption of only shorter wavelengths of solar radiation. Hence, to realize high-efficiency InGaN solar cells, the indium content in the InGaN active layer of these solar cells must be increased in order to cover a major part of the solar spectrum. Some researchers have recently proposed the use of dual nanogratings in silicon (crystalline, microcrystalline, and amorphous) and organic solar cells etc. In most of these solar cells, the nanogratings are in direct contact with the active region of the solar cells [23–31].

The ability to perform bandgap engineering with InGaN over a range that provides a good spectral match to sunlight, makes InGaN suitable for solar photovoltaic cells. It is possible to grow multiple layers with different bandgaps, as the material is relatively insensitive to defects introduced by a lattice mismatch between the layers. Metal-doped allows controlled atomic layer-by-layer growth of thin films with almost ideal characteristics enabled by strain relaxation at the first atomic layer. The crystal's lattice structures match up, resembling a perfect crystal, with corresponding luminosity. Ultrafast exciton and charge-carrier dynamics in InGaN/GaN nanowires with and without Rh/Cr_2O_3 nanoparticle decoration have been investigated using femtosecond transient absorption techniques with excitation at 415 nm and white-light probe (450–700 nm) [32]. The researchers reported on the growth and magnetic properties of single crystal Mn-doped GaN, InGaN, and AlGaN films. By optimizing the growth and annealing conditions of Mn-doped III-Nitrides, the researchers have achieved that these ferromagnetic films exhibit hysteresis [33, 34].

Furthermore, an efficient visible-light photoelectrochemical photodetector based on a compact In-rich *n*-InGaN layer activated by *p*-Cu_2O microcrystals operating as photoanode in the self-powered mode was illustrated. The excellent performance was attributed to maximized photocarrier separation in the built-in electric field of the internal *p*–*n* junction for fully depleted Cu_2O microcrystals with maximized height and the planar geometry, guaranteeing unhindered diffusion of the electrolyte to and from the photoanode surface [35].

Doping obviously reduces indium atoms composition, the aggregation of In–In and induces the deep energy level. This greatly decreases the defects and improves the valence band potential of InGaN nanorods [36]. Composites based on indium oxide containing different amounts of zinc oxide were synthesized by hydrothermal and impregnation methods. The phase composition, structure, and specific surface of the obtained composites are studied by various physicochemical methods. It was indicated that the method of formation has a significant effect on the structural characteristics of the composites, which in turn leads to the implementation of various conduction mechanisms [37, 38].

Recently, the researchers have proposed an indium-rich InGaN/GaN *p*–*i*–*n* thin-film solar cell which incorporates a dual nanograting (NG) structure: Ag nanogratings (Ag-NGs) on the backside of the solar cell and gallium nitride nanogratings (GaN–NGs) on the frontside. Finite-difference time-domain (FDTD) simulation results show that the dual NG structure couples the incident sunlight to the plasmonic and photonic modes, thereby increasing the absorption of the solar cell in a broad spectral range. It is observed that the solar cells having the dual nanograting structures have a significant enhancement in light absorption as compared to cells having either no nanogratings or having only the frontside nanogratings or only the backside nanogratings [39]. In this paper, we propose a feasible ternary semiconductor of Indium Gallium Nitride solar cell which is doped with silicon, zinc or silver. We carried out molecular modelling considering the geometrical parameters of doping atoms on the surface of $In_4Ga_4N_9$ through the absorption status and current charge density of the solar cells was studied. Moreover, the effect of a relative chemical shift between $In_4Ga_4N_9$ and doped hetero clusters of the solar cell was also investigated.

2. THEORY, MATERIALS AND COMPUTATION

The Si-, Zn-, or Ag-doped $In_4Ga_4N_9$ solar cells were calculated within the framework of first-principles calculation based on density functional theory (DFT) (Fig. 1).

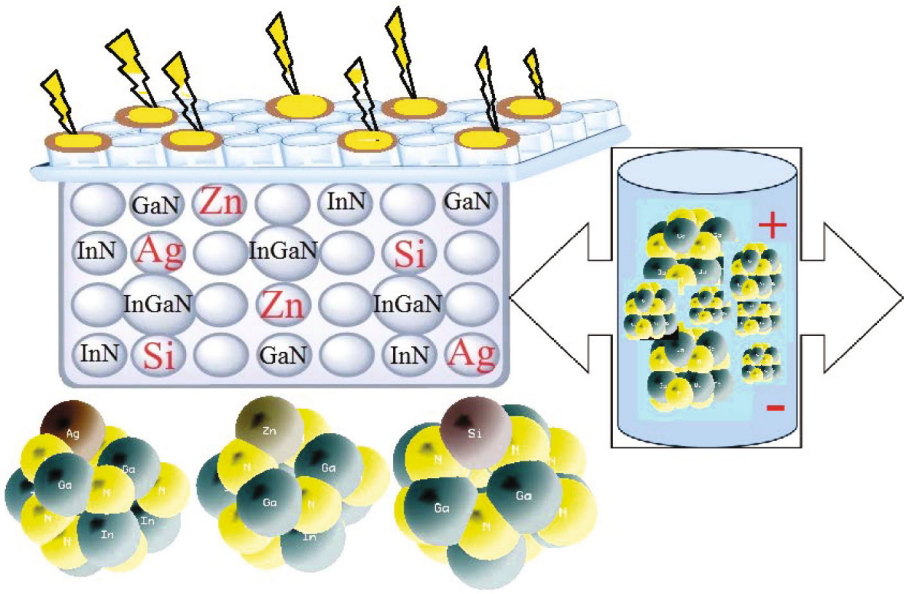

Fig. 1. Application of hetero-clusters of Ga_8N_9, In_8N_9, $In_4Ga_4N_9$, Si–$In_3Ga_4N_9$, Zn–$In_3Ga_4N_9$ and Ag–$In_3Ga_4N_9$ for energy storage in solar cells using CAM–B3LYP–D3/6-311+G(*d*, *p*) calculation.

The DFT method presents the electronic density arising from simple superposition of atomic charges ρ_{SAO}, the density obtained by full solution of DFT Kohn–Sham equation ρ_{KS} and the difference of these two:

$$\Delta\rho \equiv \rho_{KS} - \rho_{SAO}. \quad (1)$$

Any superposition of charge of separated atoms has no electric dipole moment, therefore either Kohn–Sham density ρ_{KS} or the density difference $\Delta\rho$ may be used for calculation of the polarization and the polarization induced electric field. In principle the results obtained using both approaches should differ only by an error arising from intersection of the subtracted separated atom charge by top and bottom boundaries. The coordinate shift, resulting from the periodic boundary conditions may affect magnitude of the dipole obtained from the integration over simulated volume [40–47].

The rigid potential energy surface using density functional theory [48–53] was performed due to Gaussian 16 revision C.01 program package [54] and GaussView 6.1 [55]. The coordination input for energy storage on the solar cells has applied 6-311+G(*d*, *p*) and EPR–3 basis sets. The NQR method is related to the multipole expansion in Cartesian coordinates as Eq. (2) [56, 57]:

$$V(r) = V(0) + \left[\left(\frac{\partial V}{\partial x_i}\right)_0 x_i\right] + \frac{1}{2}\left[\left(\frac{\partial^2 V}{\partial x_i x_j}\right)_0 x_i x_j\right] + \ldots. \quad (2)$$

After that, a simplification on Eq. (6), there are only the second derivatives related to the identical variable for the potential energy [48, 49, 56, 57]:

$$\begin{aligned} U &= -\frac{1}{2}\int_{\mathcal{D}} d^3 r \rho_r \left[\left(\frac{\partial^2 V}{\partial x_i^2}\right)_0 x_i^2\right] \\ &= -\frac{1}{2}\int_{\mathcal{D}} d^3 r \rho_r \left[\left(\frac{\partial E_i}{\partial x_i}\right)_0 x_i^2\right] \\ &= -\frac{1}{2}\left(\frac{\partial E_i}{\partial x_i}\right)_0 \int_{\mathcal{D}} d^3 r \left[\rho(r) x_i^2\right]. \end{aligned} \quad (3)$$

There are two parameters which must be gotten from NQR experiments: the quadrupole coupling constant, χ, and asymmetry parameter of the EFG tensor η:

$$\chi = e^2 Q q_{zz}/h, \quad (4)$$

$$\eta = q_{xx} - q_{yy}/q_{zz}, \quad (5)$$

where q_{ii} are ingredients of the EFG tensor at the quadrupole nucleus determined in the EFG principal axes system, Q is the nuclear quadrupole moment, e is the proton charge and h is the Planck's constant [58, 59].

Solid-state NMR spectroscopy is a technique for characterizing atomic level structure in solid materials such as powders, single crystals and amorphous samples and tissues. Solid-state NMR has been successfully used to study metal organic frameworks (MOFS), batteries, and surfaces of nanoporous materials [60–65].

From the DFT calculations, it has been attained the chemical shielding (CS) tensors in the principal axes

system to estimate the isotropic chemical-shielding (CSI) and anisotropic chemical-shielding (CSA) [66]:

$$\sigma_{iso} = (\sigma_{11} + \sigma_{22} + \sigma_{33})/3, \quad (6)$$

$$\sigma_{aniso} = \sigma_{33} - (\sigma_{22} + \sigma_{11})/2. \quad (7)$$

Figure 1 shows the process of energy storage on hetero-clusters of Ga_8N_9, In_8N_9, $In_4Ga_4N_9$, Si–$In_3Ga_4N_9$, Zn–$In_3Ga_4N_9$ and Ag–$In_3Ga_4N_9$ which is varied to maximize the absorption in the active region. Further, we optimized the structural parameters of nanocages of Ga_8N_9, In_8N_9, a ternary semiconductor of $In_4Ga_4N_9$solar cell which is doped with silicon, zinc or silver towards formation of hetero-clusters of Si–$In_3Ga_4N_9$, Zn–$In_3Ga_4N_9$, Ag–$In_3Ga_4N_9$ for obtaining the highest short-circuit current density in these solar cells [67–69].

3. RESULTS AND DISCUSSION

In this article, the data has evaluated the efficiency of hetero-clusters of Ga_8N_9, In_8N_9, $In_4Ga_4N_9$, Si–$In_3Ga_4N_9$, Zn–$In_3Ga_4N_9$, Ag–$In_3Ga_4N_9$ for storage energy in solar cells.

3.1. CDD, TDOS and ELF Analysis

The amounts of charge density differences "CDD" is measured by considering isolated atoms or noninteracting ones. The mentioned approximation can be the lightest to use because the superposition value may be received from the primary status of the self-consistency cycle in the code that carries out the density functional theory (Figs. 2–2f) [70]. In Fig. 2a, the atoms of N10, N12, N14, N16, N17 from Ga_8N_9 have shown the fluctuation around –9 to +4.5 Bohr. The atoms of N10, N(14), N16, N17 from In_8N_9 have indicated the fluctuation around –9 to +5 Bohr (Fig. 2b). In Fig. 2c, the atoms of N10, N14 extracted from ternary hereto-cluster of $In_4Ga_4N_9$ have exhibited the fluctuation around –9 to + 5.5 Bohr. Then, the two doped hereto-clusters of Si–$In_3Ga_4N_9$ (Fig. 2d) and Zn–$In_3Ga_4N_9$ (Fig. 2e) with active atoms of N10, N14, N16, N17 oscillated around –9 to + 2.5 Bohr. However, in doped hereto-cluster of Ag–$In_3Ga_4N_9$, except for atoms of N10, N14, N16, N17, Ag5 has been considered as a fluctuated atom around –9 to +3 Bohr (Fig. 2f).

Squirming the molecular orbital data owing to gaussian graphs of unit altitude and entire width at half maximum (FWHM) of 0.3 eV by GaussSum 3.0.2 [71] have computed total density of states (TDOS). To better understand the different adsorption characteristics by Ga_8N_9, In_8N_9, $In_4Ga_4N_9$, Si–$In_3Ga_4N_9$, Zn–$In_3Ga_4N_9$, Ag–$In_3Ga_4N_9$, TDOS has been measured. This parameter can indicate the existence of important chemical interactions often on the convex side (Figs. 3a–3f). To better understand the different adsorption characteristics of Ga_8N_9, In_8N_9, $In_4Ga_4N_9$, Si–$In_3Ga_4N_9$, Zn–$In_3Ga_4N_9$ and Ag–$In_3Ga_4N_9$, total density of states (TDOS) using Multiwfn program [72] has been measured. This parameter can indicate the existence of important chemical interactions often on the convex side (Figs. 3a–3f). In isolated system (such as molecule), the energy levels are discrete, the concept of density of state (DOS) is supposed completely valueless in this situation. Therefore, the original total DOS (TDOS) of isolated system can be written as [72]:

$$\mathrm{TDOS}(E) = \sum_i \delta(E - \epsilon_i), \quad (8)$$

$$G(x) = \frac{1}{c\sqrt{2\pi}} e^{-\frac{x^2}{2c^2}}, \quad (9)$$

where

$$c = \frac{\mathrm{FWHM}}{2\sqrt{2\ln x}}.$$

The maximum energy of TDOS for Ga_8N_9 (Fig. 3a) and In_8N_9 (Fig. 3b) with a sharp peak around –0.3 a.u. Figure 3c shows the ternary semiconductor of $In_4Ga_4N_9$ with a sharp peak around –0.3 a.u. and a weak peak around –0.4 a.u. After doping Si on $In_4Ga_4N_9$ hetero-cluster, the peak around –0.4 a.u. has been more clarified (Fig. 3d). It is remarkable that the excessive growth technique on doping silicon is a potential approach to designing high efficiency semipolar gallium nitride devices on silicon layers in a long wavelength zone. Moreover, the similar amounts of TDOS for Zn–$In_3Ga_4N_9$ with a sharper peak around –0.4 a.u. than Si–$In_3Ga_4N_9$ makes $In_4Ga_4N_9$ a more effective solar cell for adsorption energy (Fig. 3e). However, Ag–$In_3Ga_4N_9$ has shown three notable peaks around –0.28, –0.4 and –0.8 a.u. can be more efficient than $In_4Ga_4N_9$ (Fig. 3f).

Moreover, the curve map of broadened partial DOS (PDOS) and overlap DOS (OPDOS) are valuable for visualizing orbital composition analysis, PDOS function of fragment *A* is defined as:

$$\mathrm{PDOS}_A(E) = \sum_i \Xi_{i,A} F(E - \epsilon_i), \quad (10)$$

where $\Xi_{i,A}$ is the composition of fragment *A* in orbital *i*. The OPDOS between fragment *A* and *B* is defined as:

$$\mathrm{OPDOS}_{A,B}(E) = \sum_i X^i_{A,B} F(E - \epsilon_i), \quad (11)$$

where $X^i_{A,B}$ is the composition of total cross term between fragment *A* and *B* in orbital *i*.

Furthermore, a type of scalar fields called electron localization function (ELF) may demonstrate a broad span of bonding samples. Nevertheless, the distinction between deduced/raised electron delocalization/localization into cyclic π-conjugated sets stays

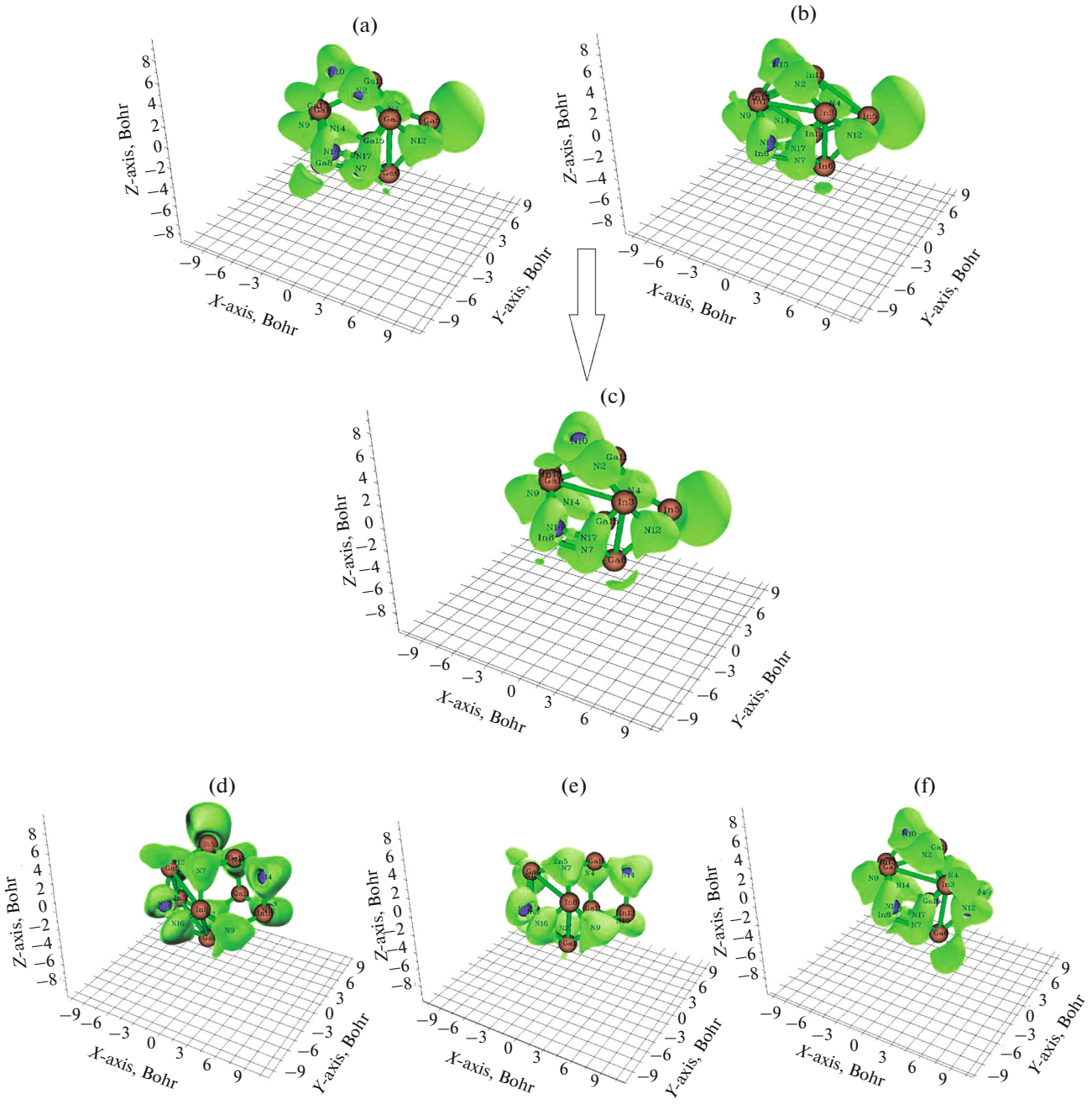

Fig. 2. CDD graphs for hetero-clusters of (a) Ga_8N_9, (b) In_8N_9, (c) $In_4Ga_4N_9$, (d) $Si–In_3Ga_4N_9$, (e) $Zn–In_3Ga_4N_9$ and (f) $Ag–In_3Ga_4N_9$.

encouraging for ELF [73]. The grosser the electron localization is in an area, the more likely the electron movement is restricted within it. Therefore, they might be discerned from the ones away if electrons are totally centralized. As Bader investigated, the zones with large electron localization possess extensive magnitudes of Fermi hole integration. But, with having a six-dimension function for the Fermi hole, it seems hard to be studied directly. Then, Becke and Edgecombe remarked that spherically averaged like spin conditional pair probability possesses a direct correlation with the Fermi hole and proposed the parameter of electron localization function (ELF) in Multiwfn program [72] and popularized for spin-polarized procedure [74]:

$$\mathrm{ELF}(r) = \frac{1}{1+[D(r)/D_0(r)]} \tag{12}$$

where

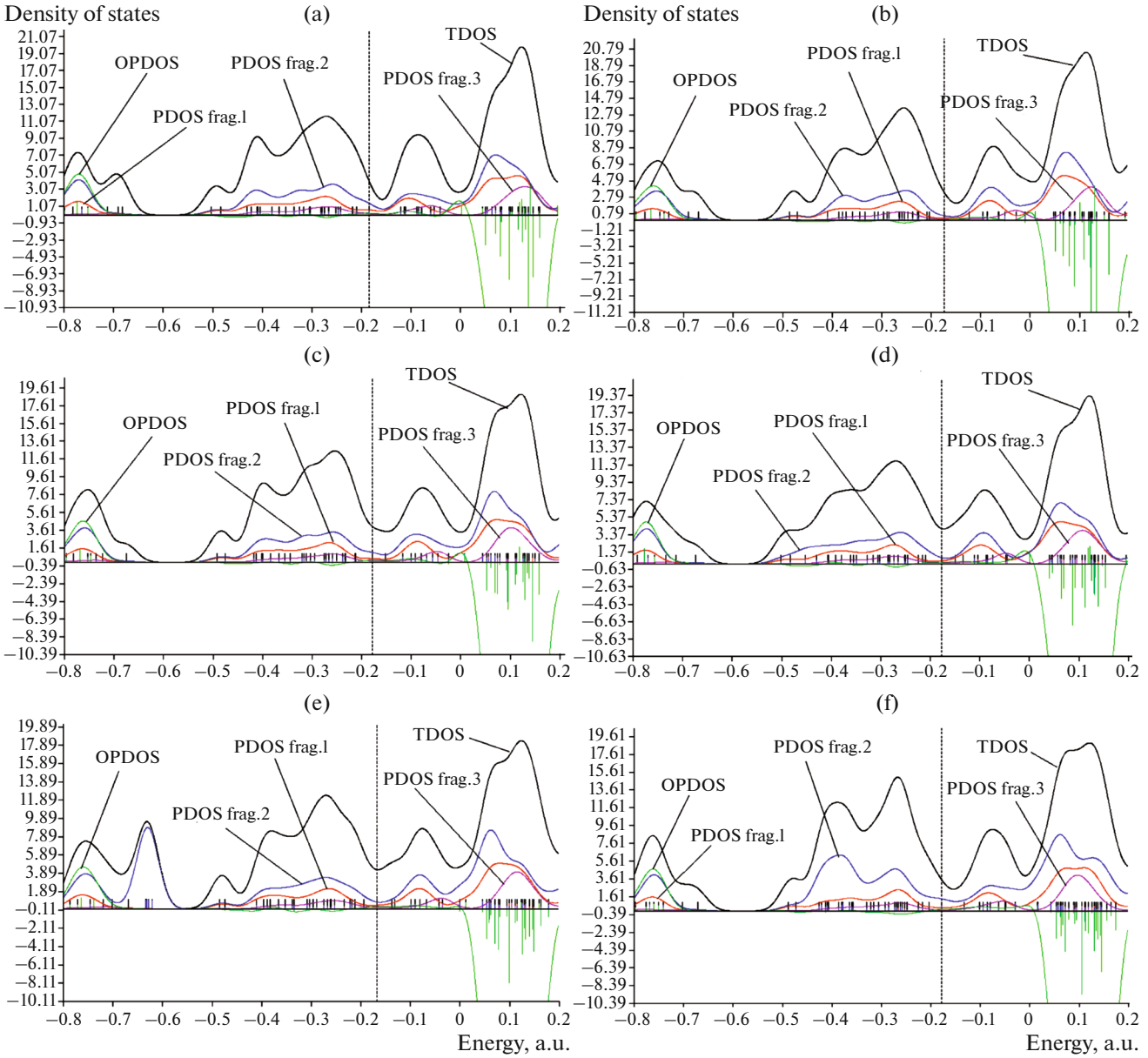

Fig. 3. TDOS graphs of hetero-clusters include (a) Ga_8N_9, (b) In_8N_9, (c) $In_4Ga_4N_9$, (d) $Si–In_3Ga_4N_9$, (e) $Zn–In_3Ga_4N_9$ and (f) $Ag–In_3Ga_4N_9$.

$$D(r)=\frac{1}{2}\sum_i \eta_i |\nabla\varphi_i(r)|^2-\frac{1}{8}\left[\frac{|\nabla\rho_\alpha(r)|^2}{\rho_\alpha(r)}+\frac{|\nabla\rho_\beta(r)|^2}{\rho_\beta(r)}\right], \quad (13)$$

and

$$D_0(r)=\frac{3}{10}\left(6\pi^2\right)^{2/3}\left[\rho_\alpha(r)^{5/3}+\rho_\beta(r)^{5/3}\right]. \quad (14)$$

For close-shell system, since $\rho_\alpha=\rho_\beta=(1/2)\rho$, D and D_0 terms can be simplified as:

$$D(r)=\frac{1}{2}\sum_i \eta_i |\nabla\varphi_i(r)|^2-\frac{1}{8}\frac{|\nabla\rho(r)|^2}{\rho(r)}, \quad (15)$$

and

$$D_0(r)=(3/10)\left(3\pi^2\right)^{2/3}\rho(r)^{5/3}. \quad (16)$$

Regarding kinetic energy, ELF was rechecked to be more punctual for both Kohn–Sham DFT and post-HF wavefunctions [75–81].

In fact, the excess kinetic energy density caused by Pauli repulsion was unfolded by $D(r)$ and $D_0(r)$ may be inspected as Thomas–Fermi kinetic energy density. Because $D_0(r)$ is brough forward the ELF as origin, what the ELF shows is an affiliate localization. The compounds of Ga_8N_9, In_8N_9, $In_4Ga_4N_9$, Si–

$In_3Ga_4N_9$, Zn–$In_3Ga_4N_9$ and Ag–$In_3Ga_4N_9$ can be defined by ELF graphs owing to exploring their delocalization/localization characterizations of electrons and chemical bonds (Figs. 4a–4f). The counter map of ELF for Ga_8N_9 and In_8N_9 has shown the electron delocalization of these two hetero-clusters based on labeling atoms of N4, Ga5, Ga15 for Ga_8N_9 (Fig. 4a) and N(4), In5, In15 for In_8N_9 (Fig. 4b), respectively. Then, formation of ternary alloy of $In_4Ga_4N_9$ indicates an isosurface map of electron delocalization due to labeling atoms of N4, In5, Ga15 (Fig. 4c). A vaster jointed area engaged by an isosurface map for Si, Zn, Ag doping $In_4Ga_4N_9$ towards formation of hetero-clusters of Si–$In_3Ga_4N_9$ (Fig. 4d), Zn–$In_3Ga_4N_9$ (Fig. 4e) and Ag–$In_3Ga_4N_9$ (Fig. 4f) due to labeling atoms of N4, Si5/Zn5/Ag5, Ga15, respectively. A narrower connected area occupied by an isosurface map means that electron delocalization is relatively difficult. However, the large counter map of ELF for Ag–$In_3Ga_4N_9$, Zn–$In_3Ga_4N_9$, Si–$In_3Ga_4N_9$ hetero-clusters can confirm that doping Ag, Zn, Si nanoparticles on the surface, respectively, increases the efficiency of ternary solar cell of $In_3Ga_4N_9$ for energy storage [82–84].

Besides, the changes of charge density analysis have illustrated that $In_3Ga_4N_9$ has shown the Bader charge of −1.131 coulomb, and after doping with silicon, zinc and silver has indicated the Bader charge of −1.172, −1.171 and −1.159 coulomb for Si–$In_3Ga_4N_9$, Zn–$In_3Ga_4N_9$, Ag–$In_3Ga_4N_9$, respectively, that describes the tensity value of these hetero-clusters for energy storage [85].

3.2. Theory of Muclear Quadrupole Resonance

The тuclear quadrupole resonance (NQR) frequencies have been measured for Ga_8N_9, In_8N_9 nanocages, ternary alloy of $In_3Ga_4N_9$ and doped hetero-clusters of Si–$In_3Ga_4N_9$, Zn–$In_3Ga_4N_9$, Ag–$In_3Ga_4N_9$ (Table 1). In this research work, the electric potential as the quantity of work energy through carrying over the electric charge from one position to another position in the essence of electric field has been evaluated for Ga_8N_9, In_8N_9 nanocages, $In_3Ga_4N_9$ ternary alloy and doped hetero-clusters of Si–$In_3Ga_4N_9$, Zn–$In_3Ga_4N_9$, Ag–$In_3Ga_4N_9$ (Table 1). In Fig. 5a, the atoms of N10, N12, N14, N16, N17 from Ga_8N_9 have shown the fluctuation in the range of −1.5 to +1 coulomb with average electric potential about −18 a.u. The atoms of N10, N14, N16, N17 from In_8N_9 have indicated the fluctuation −1.5 to +1 coulomb with average electric potential about −19 a.u (Fig. 5b). In Fig. 5c, the atoms of N10, N14 extracted from ternary hereto-cluster of $In_4Ga_4N_9$ have exhibited the fluctuation in the range of −1.5 to +1 coulomb with average electric potential about −20 a.u. Then, the Si-doped hereto-cluster of Si–$In_3Ga_4N_9$ (Fig. 5d) with active atoms of N10, N14, N16, N17 has been oscillated in the range of −1.5 to +1 coulomb with average electric potential about −20 a.u. However, in two doped hereto-clusters of Zn–$In_3Ga_4N_9$ (Fig. 5e) and Ag–$In_3Ga_4N_9$ (Fig. 5f) the atoms of N10, N14, N14, N16, N17 have been considered as fluctuated atoms between −1.5 to +1 coulomb with average electric potential about −23 a.u. In fact, by doping transition metals of Zn and Ag to $In_3Ga_4N_9$, the electric potential extracted from NQR calculations grows. Therefore, it can be proposed that doped alloys of Si–$In_3Ga_4N_9$, Zn–$In_3Ga_4N_9$ and Ag–$In_3Ga_4N_9$ might augment the ability of $In_3Ga_4N_9$ in solar cells for energy storage.

It was observed the behavior of Ga and N atoms in Ga_8N_9 (Fig. 5a) and In and N atoms in In_8N_9 (Fig. 5b) with high sensitivity based on relation coefficient of $R^2_{Ga_8N_9} = 0.9994$ and $R^2_{In_8N_9} = 0.9990$; however, ternary alloy of $In_4Ga_4N_9$ has shown the behavior of In, Ge and N atoms with high sensitivity due to relation coefficient of $R^2_{In_4Ga_4N_9} = 0.9994$ (Fig. 5c). In Fig. 5d, hetero-cluster of Si–$In_3Ga_4N_9$ has exhibited the behavior of Si-doped $In_3Ga_4N_9$ with high sensitivity of $R^2_{Si-In_4Ga_4N_9} = 0.9992$. The two hetero-clusters of Zn–$In_3Ga_4N_9$ and Ag–$In_3Ga_4N_9$ with the fluctuations of In, Ga, N and transition metals of Zn, Ag have indicated the same sensitivity graph of electric potential via charge distribution with $R^2_{Zn/Ag-In_4Ga_4N_9} = 0.9998$. On the other hand, the electrical conductivity based on NQR parameters in Table 1 can be enhanced with doping Zn (Fig. 5e) or Ag (Fig. 5f). Therefore, it can be considered that zinc and silver atoms in the functionalized Zn–$In_3Ga_4N_9$ and Ag–$In_3Ga_4N_9$ might have more impressive sensitivity for accepting the electrons in the process of energy adsorption mechanism.

3.3. Analysis of Nuclear Magnetic Resonance Spectra

Based on the resulted amounts, nuclear magnetic resonance (NMR) spectra of Ga_8N_9, In_8N_9, $In_4Ga_4N_9$, Si–$In_3Ga_4N_9$, Zn–$In_3Ga_4N_9$ and Ag–$In_3Ga_4N_9$ hetero-clusters as the potential molecules for energy storage can unravel the efficiency of these complexes in solar cells. The NMR data of isotropic (σ_{iso}) and anisotropic shielding tensors (σ_{aniso}) of Ga_8N_9, In_8N_9 nanocages, ternary alloy of $In_3Ga_4N_9$ and doped hetero-clusters of Si–$In_3Ga_4N_9$, Zn–$In_3Ga_4N_9$, Ag–$In_3Ga_4N_9$ have been computed by Gaussian 16 revision C.01 program package [40] and been shown in Table 2. In Table 2, NMR data has reported the notable amounts for Ga_8N_9, In_8N_9, $In_4Ga_4N_9$, Si–$In_3Ga_4N_9$, Zn–$In_3Ga_4N_9$ and Ag–$In_3Ga_4N_9$ hetero-clusters. The notable fragile signal intensity close to the parallel edge of the nanocluster sample might be owing to indium or gallium binding induced non-spherical distribution of Ga_8N_9 and In_8N_9, nanocages

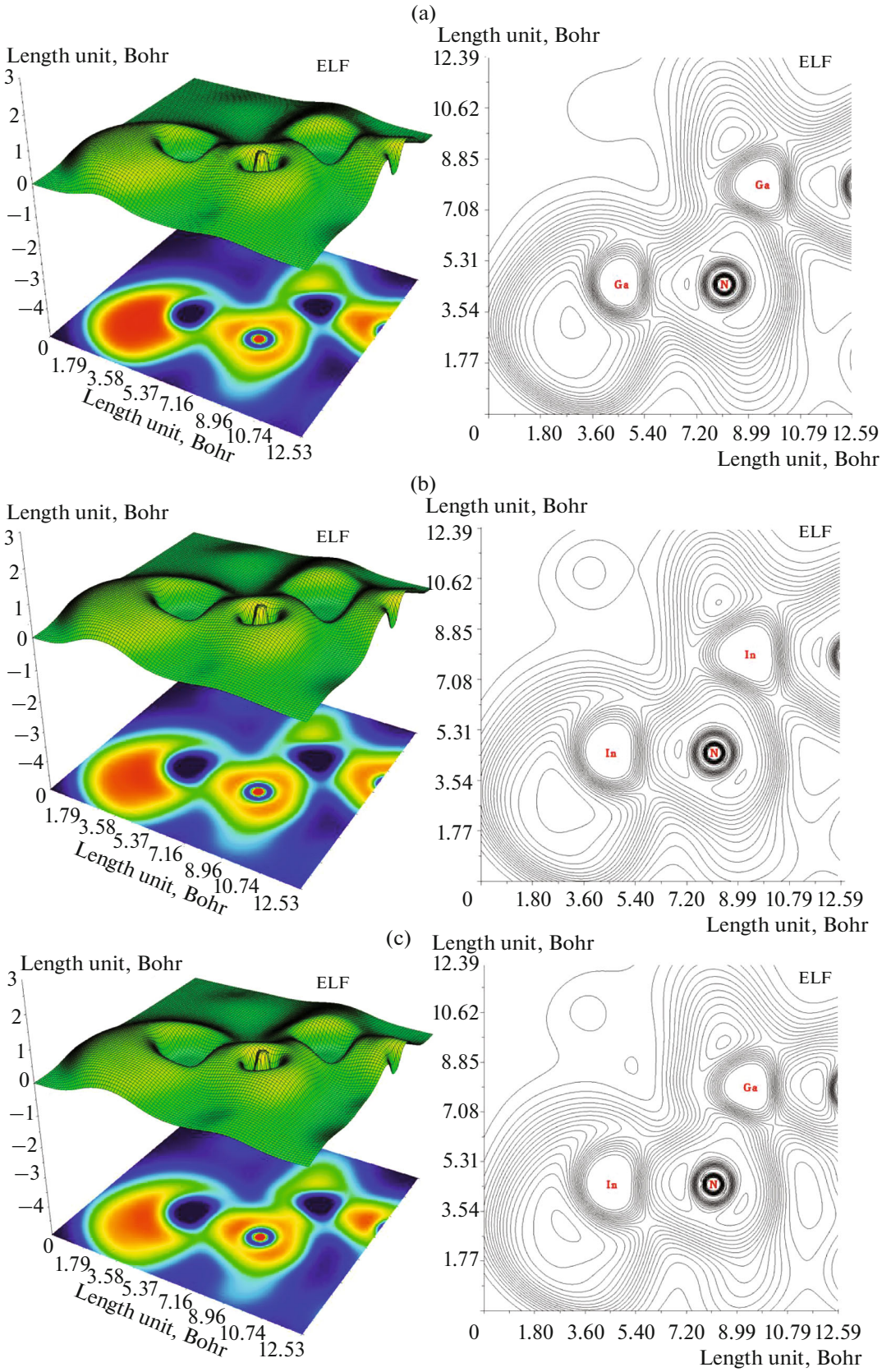

Fig. 4. The graphs of ELF for hetero-clusters include (a) Ga_8N_9, (b) In_8N_9, (c) $In_4Ga_4N_9$, (d) $Si–In_3Ga_4N_9$, (e) $Zn–In_3Ga_4N_9$ and (f) $Ag–In_3Ga_4N_9$. (Counter line map in the right and shaded surface map with projection in the left).

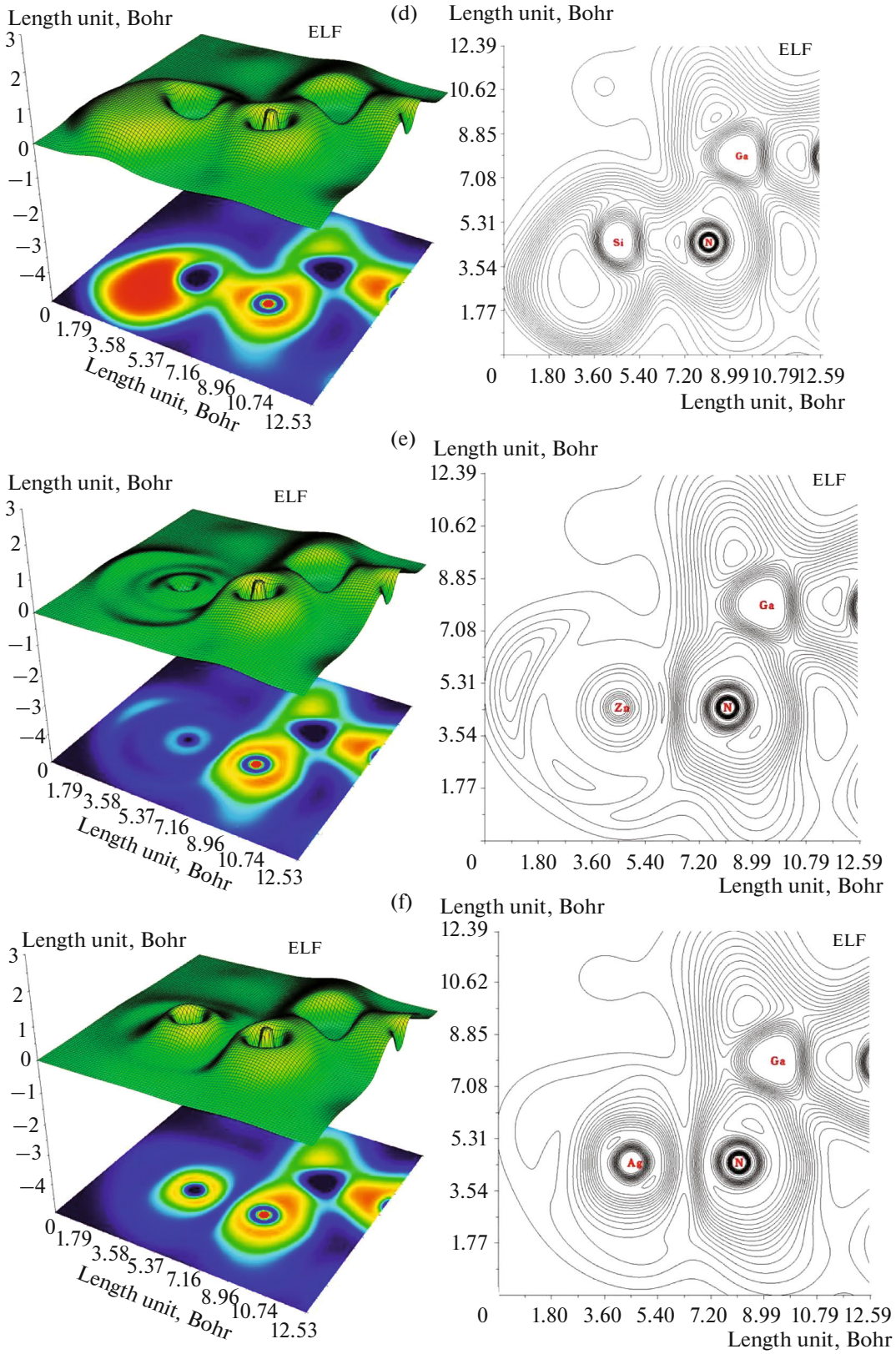
(d)
Length unit, Bohr
ELF
3
2
1
0
−1
−2
−3
−4
0
1.79
3.58
5.37
7.16
8.96
10.74
12.53
Length unit, Bohr
Length unit, Bohr
ELF
12.39
10.62
8.85
7.08
5.31
3.54
1.77
Ga
Si
N
0
1.80
3.60
5.40
7.20
8.99
10.79
12.59
Length unit, Bohr
(e)
Length unit, Bohr
Length unit, Bohr
ELF
Ga
Zn
N
(f)
Length unit, Bohr
Length unit, Bohr
ELF
Ga
Ag
N

Fig. 4. (Contd.)

Table 1. The electric potential (E_p/a.u.) and Bader charge (Q/coulomb) through NQR calculation for hetero-clusters of Ga_8N_9, In_8N_9, $In_4Ga_4N_9$, $Si–In_3Ga_4N_9$, $Zn–In_3Ga_4N_9$ and $Ag–In_3Ga_4N_9$

	Ga_8N_9		In_8N_9			$In_4Ga_4N_9$		
atom	Q	E_p	atom	Q	E_p	atom	Q	E_p
Ga1	1.02	−1.24	In1	1.09	−1.12	Ga1	0.97	−1.25
N2	−1.07	−18.40	N2	−1.11	−18.44	N2	−1.07	−18.42
Ga3	1.02	−1.23	In3	1.06	−1.12	In3	1.09	−1.12
N4	−1.09	−18.41	N4	−1.08	−18.46	N4	−1.05	−18.44
Ga5	0.74	−1.25	In5	0.75	−1.14	In5	0.84	−1.13
Ga6	1.02	−1.23	In6	1.04	−1.12	Ga6	0.94	−1.25
N7	−1.07	−18.40	N7	−1.10	−18.45	N7	−1.07	−18.42
Ga8	1.02	−1.24	In8	1.10	−1.13	In8	1.13	−1.12
N9	−1.06	−18.41	N9	−1.08	−18.46	N9	−1.09	−18.44
N10	−0.70	−18.41	N10	−0.76	−18.46	N10	−0.71	−18.41
Ga11	1.06	−1.24	In11	1.10	−1.13	Ga11	0.96	−1.25
N12	−1.06	−18.40	N12	−1.07	−18.45	N12	−1.05	−18.44
Ga13	0.97	−1.25	In13	1.00	−1.15	In13	1.04	−1.13
N14	−0.70	−18.41	N14	−0.82	−18.47	N14	−0.73	−18.41
Ga15	1.06	−1.24	In15	1.06	−1.14	Ga15	0.96	−1.25
N16	−0.57	−18.35	N16	−0.60	−18.39	N16	−0.59	−18.37
N17	−0.57	−18.35	N17	−0.60	−18.39	N17	−0.58	−18.38
	$Si–In_3Ga_4N_9$			$Zn–In_3Ga_4N_9$			$Ag–In_3Ga_4N_9$	
atom	Q	E_p	atom	Q	E_p	atom	Q	E_p
Ga1	1.01	−1.23	Ga1	0.98	−1.24	Ga1	1.00	−1.24
N2	−1.10	−18.40	N2	−1.07	−18.42	N2	−1.10	−18.42
In3	1.13	−1.11	In3	1.08	−1.13	In3	1.07	−1.13
N4	−1.10	−18.41	N4	−1.05	−18.43	N4	−0.99	−18.40
Si5	0.74	−1.90	Zn5	0.81	−16.25	Ag5	0.44	−17.86
Ga6	0.96	−1.24	Ga6	0.94	−1.25	Ga6	0.94	−1.26
N7	−1.07	−18.41	N7	−1.09	−18.42	N7	−1.10	−18.42
In8	1.17	−1.11	In8	1.17	−1.11	In8	1.16	−1.11
N9	−1.07	−18.43	N9	−1.06	−18.44	N9	−1.10	−18.43
N10	−0.75	−18.42	N10	−0.73	−18.43	N10	−0.72	−18.42
Ga11	1.10	−1.242	Ga11	0.99	−1.26	Ga11	1.06	−1.24
N12	−1.09	−18.41	N12	−1.05	−18.43	N12	−0.91	−18.43
In13	1.05	−1.13	In13	1.02	−1.14	In13	1.08	−1.12
N14	−0.75	−18.42	N14	−0.77	−18.43	N14	−0.73	−18.42
Ga15	1.02	−1.24	Ga15	0.99	−1.26	Ga15	1.07	−1.24
N16	−0.60	−18.36	N16	−0.58	−18.36	N16	−0.61	−18.37
N17	−0.57	−18.36	N17	−0.56	−18.36	N17	−0.55	−18.38

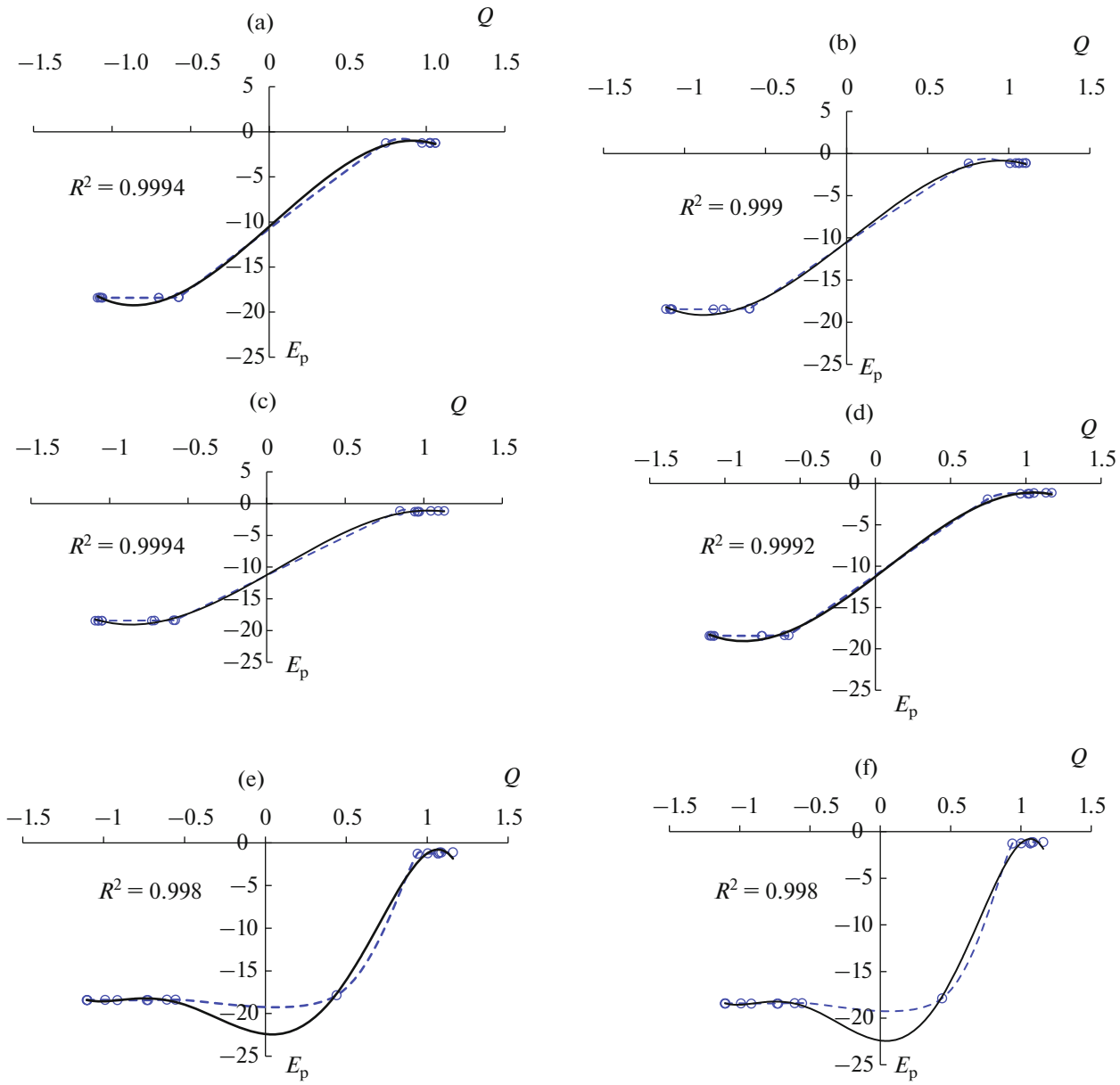

Fig. 5. Electric potential (a.u.) versus Bader charge (coulomb) through NQR calculation for hetero-clusters of (a) Ga_8N_9, (b) In_8N_9, (c) $In_4Ga_4N_9$, (d) $Si–In_3Ga_4N_9$, (e) $Zn–In_3Ga_4N_9$ and (f) $Ag–In_3Ga_4N_9$.

and $In_4Ga_4N_9$ hetero cluster. Figures 6a–6f exhibited the same tendency of shielding for indium or gallium; however, a considerable deviation exists from doping atoms of silicon, zinc and silver as electron acceptors on the surface of $In_4Ga_4N_9$ hetero-cluster.

The observed increase in the chemical shift anisotropy spans for nanocages of Ga_8N_9 (Fig. 6a) and In_8N_9 (Fig. 6b) is near N10, N14, N16, and N17. The yield of electromagnetic shifting can be directed by nitrogen atoms of N10 and N14 extracted from ternary hereto-cluster of $In_4Ga_4N_9$ (Fig. 6c). Figure 6d has shown that the intensity for energy storage can be enhanced in $Si–In_3Ga_4N_9$ due to oscillating of chemical shielding in N10, N14, N16, N17 atoms. The atoms of N10, N4, N14, N16, N17 have indicated the fluctuation in chemical shielding for $Zn–In_3Ga_4N_9$ (Fig. 6e) and $Ag–In_3Ga_4N_9$ (Fig. 6f). So, it can be observed that doped hetero-clusters of $Si–In_3Ga_4N_9$, $Zn–In_3Ga_4N_9$ and $Ag–In_3Ga_4N_9$ might ameliorate the capability of $In_4Ga_4N_9$ in solar cells for energy storage.

3.4. Insight of Infrared Spectroscopy and Thermochemistry

The infrared spectroscopy (IR) has been performed for Ga_8N_9, In_8N_9 nanocages, ternary alloy of

Table 2. Data of NMR shielding tensors (ppm) for selected atoms of hetero-clusters containing Ga_8N_9, In_8N_9, $In_4Ga_4N_9$, $Si–In_3Ga_4N_9$, $Zn–In_3Ga_4N_9$ and $Ag–In_3Ga_4N_9$

Ga_8N_9			In_8N_9			$In_4Ga_4N_9$		
atom	σ_{iso}	σ_{aniso}	atom	σ_{iso}	σ_{aniso}	atom	σ_{iso}	σ_{aniso}
Ga1	10.00	7.22	In1	8.97	9.34	Ga1	6.35	14.81
N2	65.17	155.17	N2	108.17	231.70	N2	49.37	1236.98
Ga3	7.40	5.38	In3	9.39	8.09	In3	10.05	6.27
N4	0.90	198.14	N4	122.41	219.98	N4	407.86	737.17
Ga5	2.20	8.57	In5	10.67	5.90	In5	10.77	14.12
Ga6	7.40	5.40	In6	9.77	4.05	Ga6	7.13	11.63
N7	65.47	154.46	N7	60.40	239.64	N7	158.31	1243.03
Ga8	10.01	7.17	In8	9.00	10.07	In8	11.07	11.35
N9	87.27	157.79	N9	27.45	274.28	N9	271.94	914.87
N10	962.13	1264.69	N10	1103.69	1399.68	N10	2443.15	30749.20
Ga11	1.96	11.20	In11	1.27	13.28	Ga11	0.65	159.31
N12	181.84	386.93	N12	17.23	108.52	N12	21.72	371.05
Ga13	1.54	20.65	In13	0.54	14.84	In13	103.61	276.00
N14	961.95	1263.86	N14	428.77	783.32	N14	2062.36	25680.51
Ga15	1.98	11.20	In15	6.31	7.91	Ga15	27.53	130.61
N16	146.78	296.04	N16	189.53	412.00	N16	149.91	453.17
N17	185.78	358.96	N17	212.86	452.62	N17	193.31	401.49
$Si–In_3Ga_4N_9$			$Zn–In_3Ga_4N_9$			$Ag–In_3Ga_4N_9$		
atom	σ_{iso}	σ_{aniso}	atom	σ_{iso}	σ_{aniso}	atom	σ_{iso}	σ_{aniso}
Ga1	22.45	78.49	Ga1	9.33	37.46	Ga1	4.28	11.20
N2	90.54	2353.70	N2	229.69	1052.37	N2	90.87	242.42
In3	0.59	36.86	In3	14.55	13.20	In3	9.12	4.92
N4	352.52	741.52	N4	44.34	780.90	N4	206.13	466.97
Si5	34.54	70.55	Zn5	96.00	131.08	Ag5	131.61	127.73
Ga6	14.68	34.86	Ga6	6.52	11.60	Ga6	6.39	4.73
N7	36.18	1582.14	N7	67.56	506.30	N7	101.49	225.88
In8	6.44	31.57	In8	15.88	24.88	In8	6.89	10.56
N9	66.74	1817.15	N9	499.24	1720.50	N9	8.73	387.11
N10	21230.98	62643.40	N10	9100.06	20128.37	N10	1002.27	1666.74
Ga11	53.30	480.09	Ga11	1.26	182.44	Ga11	3.11	16.42
N12	22.84	554.17	N12	143.78	889.40	N12	185.61	661.73
In13	236.73	423.81	In13	67.19	124.27	In13	5.06	22.95
N14	5858.91	55100.56	N14	2466.42	15963.10	N14	1016.95	1694.91
Ga15	36.74	410.71	Ga15	17.30	118.62	Ga15	3.80	15.59
N16	84.83	3132.38	N16	1537.43	5335.54	N16	106.33	303.31
N17	632.77	5076.17	N17	687.25	4281.88	N17	224.91	360.96

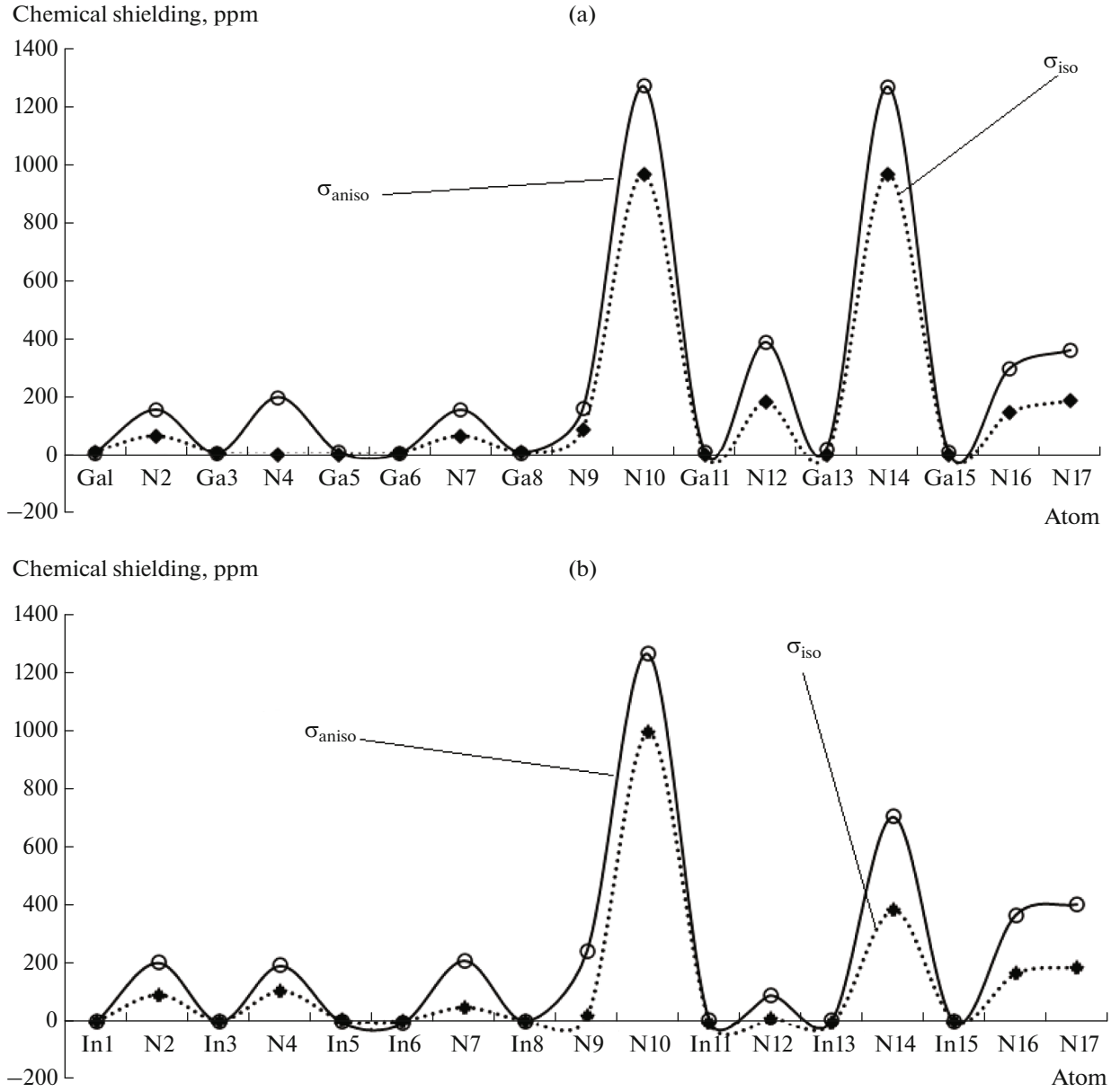

Fig. 6. The NMR spectra for hetero-clusters of (a) Ga_8N_9, (b) In_8N_9, (c) $In_4Ga_4N_9$, (d) $Si–In_3Ga_4N_9$, (e) $Zn–In_3Ga_4N_9$ and (f) $Ag–In_3Ga_4N_9$.

$In_3Ga_4N_9$ and doped hetero-clusters of $Si–In_3Ga_4N_9$, $Zn–In_3Ga_4N_9$, $Ag–In_3Ga_4N_9$ (Figs. 7a–7f). Therefore, it has been simulated the several clusters containing Ga_8N_9 (Fig. 7a), In_8N_9 (Fig. 7b), $In_3Ga_4N_9$ (Fig. 7c), $Si–In_3Ga_4N_9$ (Fig. 7d), $Zn–In_3Ga_4N_9$ (Fig. 7e), and $Ag–In_3Ga_4N_9$ (Fig. 7f). The frequency values through the IR curves between 100–1200 cm^{-1} have been achieved for Ga_8N_9 with several sharp peaks around 391.27, 420.84, 451.72, 581.93, 624.62, 686.54 and 692.45 cm^{-1} (Fig. 7a). Figure 7b has shown the frequency range between 100–1200 cm^{-1} for In_8N_9 with sharp peaks around 356.43, 385.93, 409.88, 416.57, 493.70 and 749.78 cm^{-1}. Figure 7c has indicated the fluctuation of frequency between 100–1200 cm^{-1} for $In_4Ga_4N_9$ with sharp peaks around 386.14, 388.65, 450.05, 464.72 and 844.38 cm^{-1}. The graph of Fig. 7d has been observed in the frequency range between 200–1100 cm^{-1} for $Si–In_3Ga_4N_9$ with several sharp peaks around 372.66, 377.37, 425.97, 643.15, 658.78, 814.28 and 1001.62 cm^{-1}. Figure 7e has shown the frequency range between 100–1100 cm^{-1} for $Zn–In_3Ga_4N_9$ with sharp peaks around 344.39, 363.95, 374.21, 391.72, 443.55, 660.86, 689.18, 808.93 and 953.51 cm^{-1}. Furthermore, the graph of Fig. 7f has

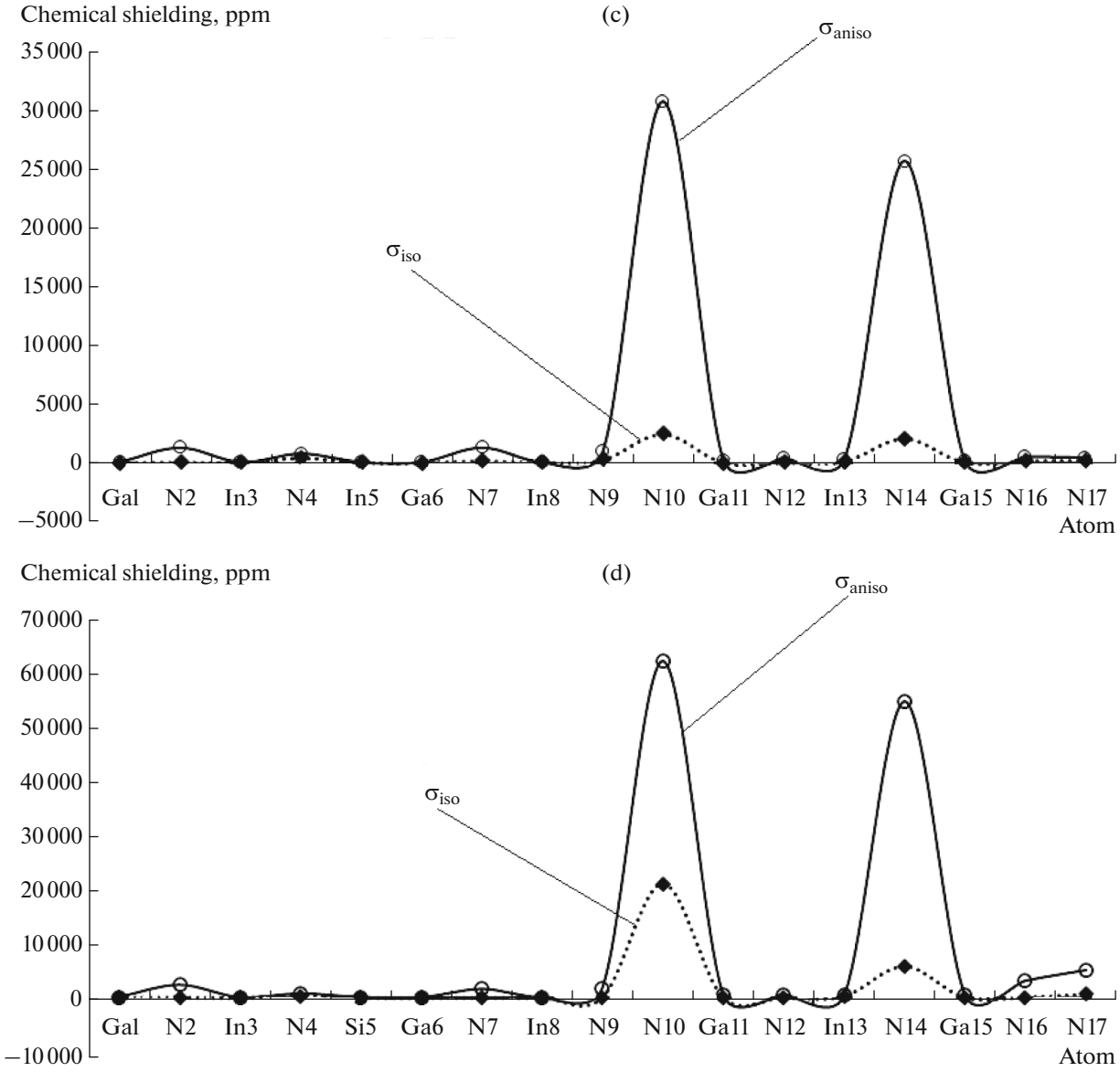

Fig. 6. (Contd.)

been observed in the frequency range between 100–1200 cm^{-1} for Ag–$In_3Ga_4N_9$ with several sharp peaks around 364.05, 392.08, 421.72, 720.67, 749.85 and 841.15 cm^{-1}.

Energy storage with hetero-clusters has described that the frame of the overcoming cluster is related to Ag–$In_3Ga_4N_9$ in the high amounts of frequency. This property makes Ag–$In_3Ga_4N_9$ potentially advantageous for certain high-frequency applications requiring solar cells for energy storage. The advantages of silver over indium gallium nitride include its higher electron and hole mobility, allowing silver doping devices to operate at higher frequencies than silicon and zinc doping devices.

Table 3 through the thermodynamic specifications concluded that hetero-clusters of Ga_8N_9, In_8N_9, $In_4Ga_4N_9$, Si–$In_3Ga_4N_9$, Zn–$In_3Ga_4N_9$ and Ag–$In_3Ga_4N_9$ might be more efficient structure for energy storage in the solar cells. Thermodynamic parameters of hetero-clusters of Ga_8N_9, In_8N_9, $In_4Ga_4N_9$, Si–$In_3Ga_4N_9$, Zn–$In_3Ga_4N_9$ and Ag–$In_3Ga_4N_9$ have been assigned through doping of ternary nanocluster of $In_4Ga_4N_9$ with Si, Zn and Ag towards formation hetero-clusters (Table 3).

The adsorption efficiency of Ga_8N_9, In_8N_9, $In_4Ga_4N_9$, Si–$In_3Ga_4N_9$, Zn–$In_3Ga_4N_9$ and Ag–$In_3Ga_4N_9$ based on dipole moment has been evaluated by the ΔG_f^o. The changes of Gibbs free energy versus

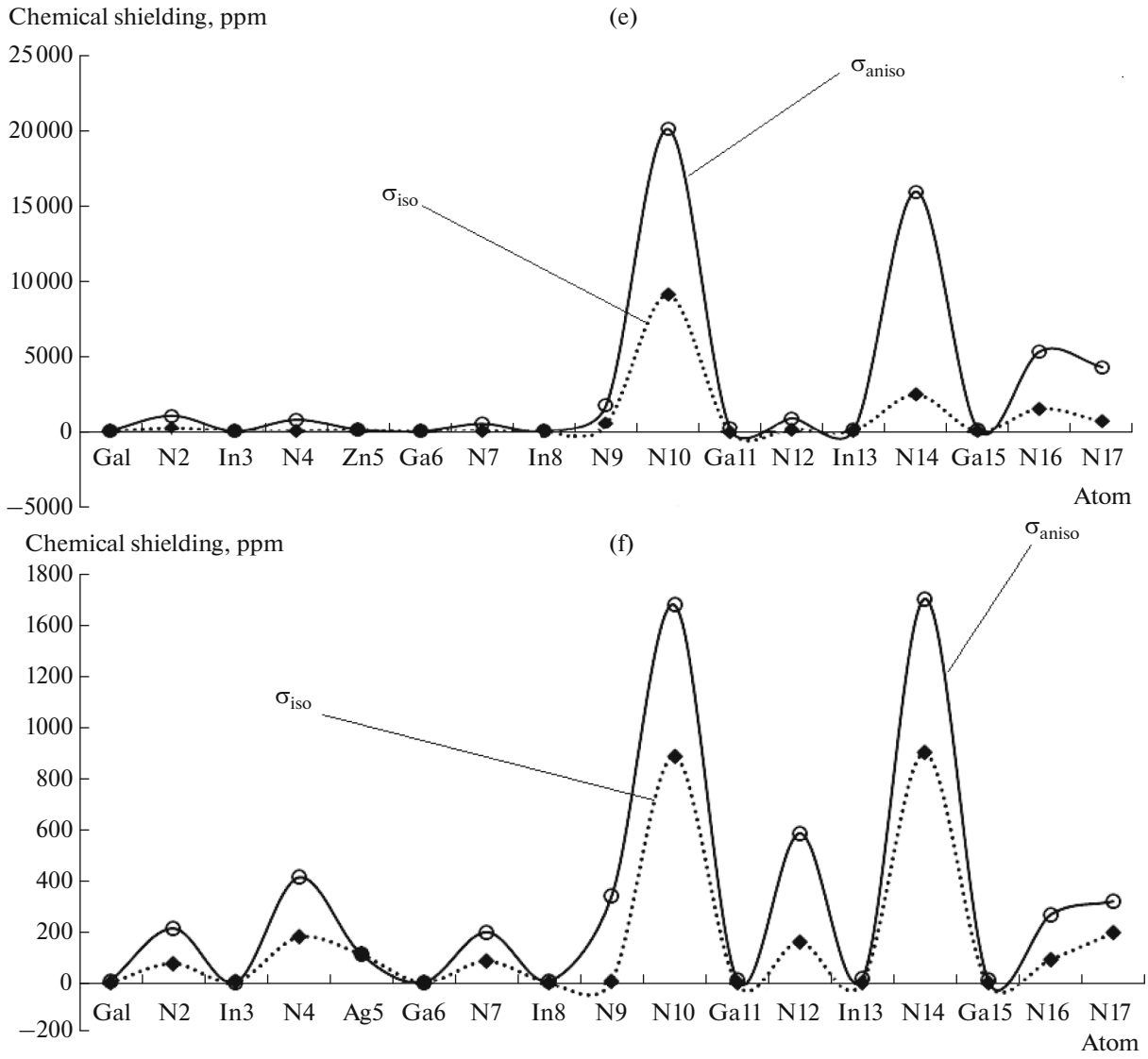

Fig. 6. (Contd.)

dipole moment could detect the maximum efficiency of Ag–$In_3Ga_4N_9$ hetero-cluster for energy storage in the solar cells through $\Delta G^{o}_{f,Ag-In_3Ga_4N_9} = -409.008 \times 10^3$ kcal/mol (Table 3). Moreover, in InGaN, the photo excited electrons and holes are strongly bounded by the excitons because of their large exciton binding energy as $E^{o}_{Ag-In_3Ga_4N_9} > E^{o}_{Zn-In_3Ga_4N_9} > E^{o}_{Si-In_3Ga_4N_9}$ due to its efficient exciton dissociation (Table 3).

The solar cells formed by Ga_8N_9, In_8N_9, $In_4Ga_4N_9$, Si–$In_3Ga_4N_9$, Zn–$In_3Ga_4N_9$ and Ag–$In_3Ga_4N_9$ feature a hierarchical structure with the electron donor/acceptor layer sandwiched by anode and cathode, which raises the importance of controlling the molecular crystal orientation, domain size, and vertical distribution to facilitate the charge collection at electrodes. Doping obviously reduces indium atoms composition, the aggregation of In–In and induces the deep energy level. This greatly decreases the defects and improves the valence band potential of $In_3Ga_4N_9$ nanorods. In this paper, we have demonstrated that the ternary semiconductor of Indium Gallium Nitride structure can lead to a significant absorption enhancement in a broad spectral range of incident light in the presence of zinc and silver. A comparison between solar cells containing Si-, Zn- or Ag-doped $In_3Ga_4N_9$ shows that the solar cells containing Zn or Ag structures show a more enhanced solar cell performance than the solar cells containing only the single $In_3Ga_4N_9$ structure. This efficient doping strategy not only bridges the gaps of heteroatom doped $In_3Ga_4N_9$ based photoelectrodes, but also can provide deep

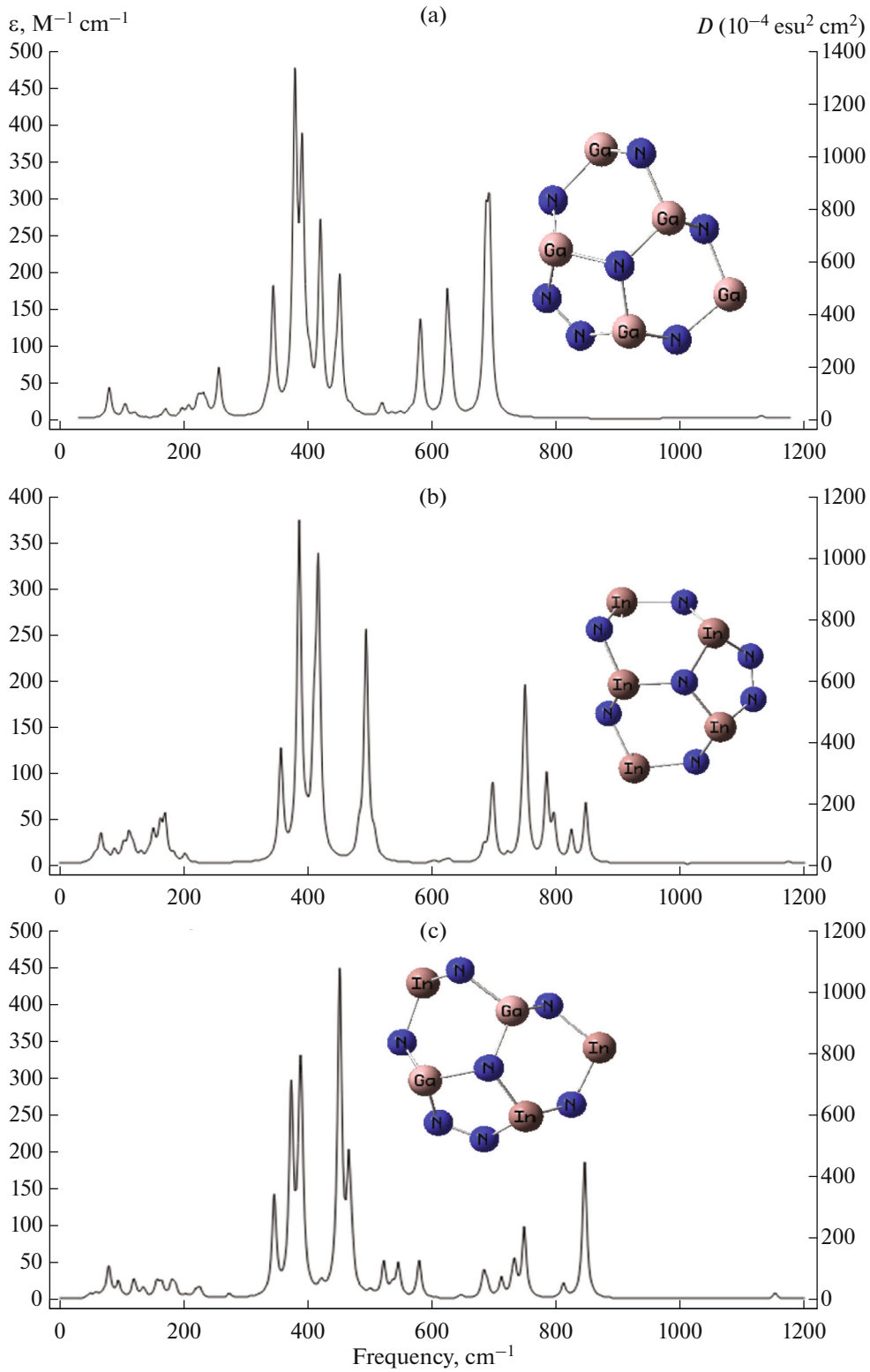

Fig. 7. The frequency (cm^{-1}) changes through the IR spectra for hetero-clusters of (a) Ga_8N_9, (b) In_8N_9, (c) $In_4Ga_4N_9$, (d) Si–$In_3Ga_4N_9$, (e) Zn–$In_3Ga_4N_9$ and (f) Ag–$In_3Ga_4N_9$.

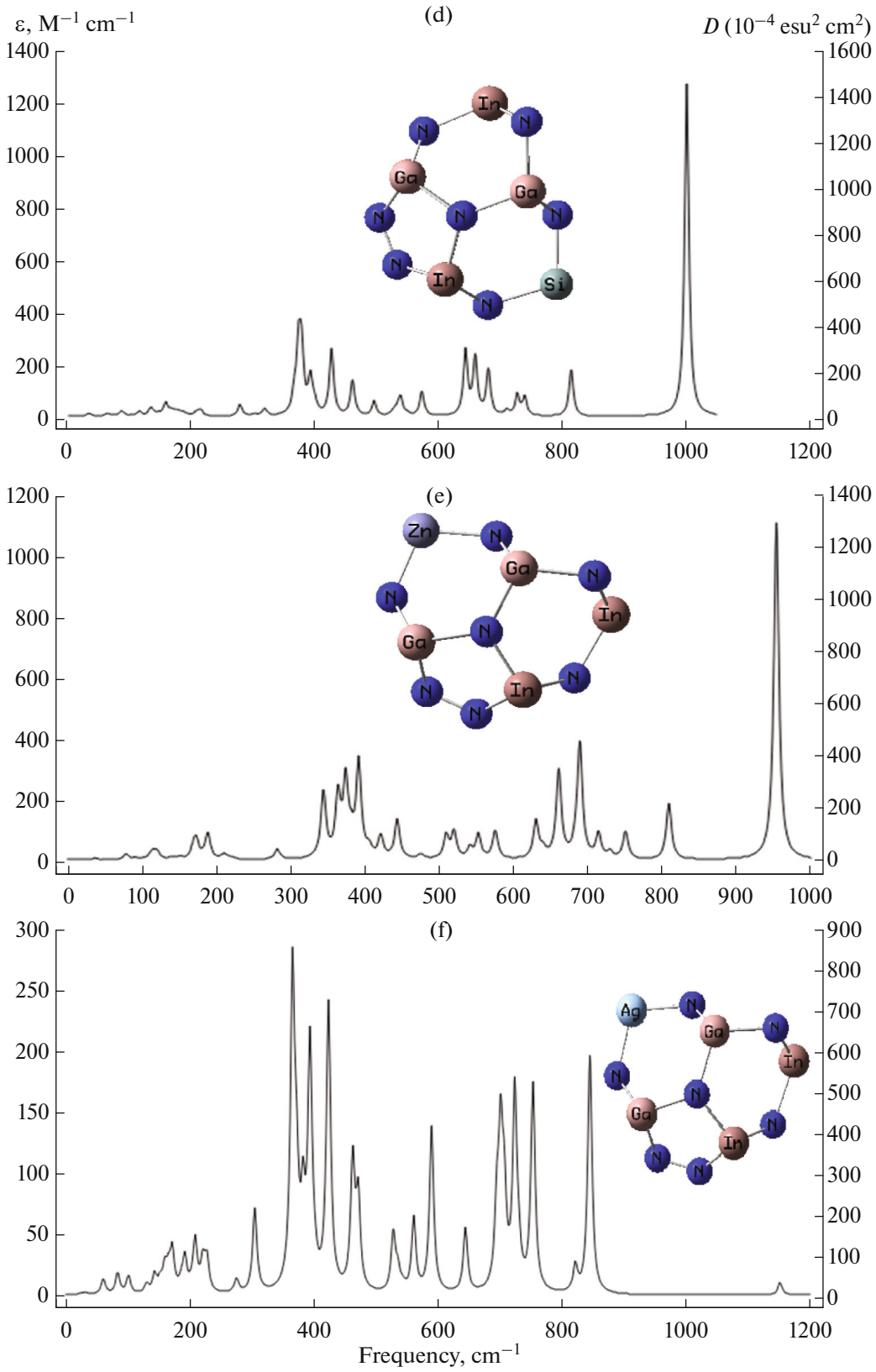

Fig. 7. (Contd.)

Table 3. The thermodynamic characters of hetero-clusters of Ga_8N_9, In_8N_9, $In_4Ga_4N_9$, Si–$In_3Ga_4N_9$, Zn–$In_3Ga_4N_9$ and Ag–$In_3Ga_4N_9$ using CAM–B3LYP–D3/6-311+G(*d*, *p*) calculation

Compound	Dipole moment, Debye	$\Delta E_f^o \times 10^{-3}$, kcal/mol	$\Delta H_f^o \times 10^{-3}$, kcal/mol	$\Delta G_f^o \times 10^{-3}$, kcal/mol	S_{ads}^o, cal/K mol	$E_{atom\text{-}doping}^o$, kcal/mol
Ga_8N_9	4.7174	–319.300	–319.299	–319.344	149.170	–
In_8N_9	6.3277	–318.223	–318.222	–318.266	147.236	–
$In_4Ga_4N_9$	4.6709	–318.743	–318.743	–318.788	151.994	–
Si–$In_3Ga_4N_9$	6.2553	–319.979	–319.978	–320.023	150.570	–1.236
Zn–$In_3Ga_4N_9$	5.9528	–358.610	–358.609	–358.655	151.603	–39.867
Ag–$In_3Ga_4N_9$	2.9453	–408.962	–408.962	–409.008	154.357	–90.219

insights into controlling the electronic structure for enhanced solar converting efficiency [86].

4. CONCLUSIONS

In this investigation, it has been provided a ternary semiconductor of Indium Gallium Nitride solar cell which is doped with silicon, zinc or silver. Energy grabbing on the hetero-clusters of Ga_8N_9, In_8N_9, $In_4Ga_4N_9$, Si–$In_3Ga_4N_9$, Zn–$In_3Ga_4N_9$, Ag–$In_3Ga_4N_9$ as solar cells was investigated by first-principles calculations. The effect of a relative chemical shift between $In_4Ga_4N_9$ and doped hetero clusters of the solar cell was also investigated. Thermodynamic parameters have constructed a detailed molecular model for atom–atom interactions and a distribution of point charges which can be utilized to reproduce the polarity of the solid material and the adsorbing molecules. In InGaN, the photo excited electrons and holes are strongly bounded by the excitons because of their large exciton binding energy as $E^o_{Ag-In_3Ga_4N_9} > E^o_{Zn-In_3Ga_4N_9} > E^o_{Si-In_3Ga_4N_9}$ due to its efficient exciton dissociation.

This property makes Ag–$In_3Ga_4N_9$ potentially advantageous for certain high-frequency applications requiring solar cells for energy storage. The advantages of silver over indium gallium nitride include its higher electron and hole mobility, allowing silver doping devices to operate at higher frequencies than silicon and zinc doping devices through $\Delta G^o_{f,Ag-In_3Ga_4N_9} = -409.008 \times 10^3$ kcal/mol. The two hetero-clusters of Zn–$In_3Ga_4N_9$ and Ag–$In_3Ga_4N_9$ with the fluctuations of In, Ga, N and transition metals of Zn, Ag have indicated the same sensitivity graph of electric potential via charge distribution with $R^2_{Zn/Ag-In_4Ga_4N_9} = 0.9998$. On the other hand, the electrical conductivity based on NQR parameters in can be enhanced with doping Zn or Ag. The advantages of silver over indium gallium nitride include its higher electron and hole mobility, allowing silver doping devices to operate at higher frequencies than silicon and zinc doping devices. Thus, it should be explored its unique properties, such as its ability to increase energy storage which could lead to advancements solar cells.

ACKNOWLEDGMENTS

In successfully completing this paper and its research, the authors are grateful to Kastamonu University.

FUNDING

This work was supported by ongoing institutional funding. No additional grants to carry out or direct this particular research were obtained.

CONFLICT OF INTEREST

The authors of this work declare that they have no conflicts of interest.

REFERENCES

1. A. Di Carlo, Physica Status Solidi A **183**, 81–85 (2001). https://doi.org/10.1002/1521-396X(200101)183:1<81::AID-PSSA81>3.0.CO;2-N
2. Y. Arakawa, IEEE J. Select. Top. Quantum Electron. **8**, 823–832 (2002). https://doi.org/10.1109/JSTQE.2002.801675
3. L. V. Lukin, Russ. J. Phys. Chem. B **17**, 1300–1308 (2023). https://doi.org/10.1134/S1990793123060180
4. M. G. Golubkov, A. V. Dmitriev, A. V. Suvorova, et al., Russ. J. Phys. Chem. B **16**, 537–542 (2022). https://doi.org/10.1134/S199079312203006X
5. Q. Meng, Q. Lin, F. Han, et al., Materials **14**, 6193 (2021). https://doi.org/10.3390/ma14206193
6. F. Mollaamin and M. Monajjemi, Russ. J. Phys. Chem. B **18**, 1199–1216 (2024). https://doi.org/10.1134/S1990793124700519
7. M. Monajjemi, F. Mollaamin, S. Shahriari, et al., Russ. J. Phys. Chem. B **18**, 1090–1112 (2024). https://doi.org/10.1134/S1990793124700465

8. F. Mollaamin and M. Monajjemi, Russ. J. Phys. Chem. B **18**, 1177–1198 (2024). https://doi.org/10.1134/S1990793124700507
9. H. Amano, N. Sawaki, I. Akasaki, et al., Appl. Phys. Lett. **48**, 353 (1986). https://doi.org/10.1063/1.96549
10. F. Mollaamin and M. Monajjemi, Russ. J. Phys. Chem. B **18**, 533–548 (2024). https://doi.org/10.1134/S199079312402012X
11. H. Amano, M. Kito, K. Hiramatsu, et al., Jpn. J. Appl. Phys. **28**, L2112 (1989). https://doi.org/10.1143/JJAP.28.L2112
12. H. Amano, T. Asahi, and I. Akasaki, Jpn. J. Appl. Phys. **29**, L205(1990). https://doi.org/10.1143/JJAP.29.L205
13. I. Akasaki, H. Amano, S. Sota, et al., Jpn. J. Appl. Phys. **34**, L1517 (1995). https://doi.org/10.7567/JJAP.34.L1517
14. M. Kodama, M. Sugimoto, E. Hayashi, et al., Appl. Phys. Express **1**, 021104 (2008). https://doi.org/10.1143/APEX.1.021104
15. M. Wraback, H. Shen, J. C. Carrano, et al., Appl. Phys. Lett. **76**, 1155–1157 (2000). https://doi.org/10.1063/1.125968
16. R. J. Bashirov, N. E. Ismayilov, R. E. Huseynov et al., Adv. Phys. Res. **6**, 90–99 (2024). https://doi.org/10.62476/apr62.90
17. Sh. B. Utamuradova, Sh. Kh. Daliev, B. R. Bokiev, et al., Adv. Phys. Res. **6**, 211–218 (2024). https://doi.org/10.62476/apr63211
18. Sh. B. Utamuradova, D. A. Rakhmanov, P. L. Tuan, et al., Adv. Phys. Res. **6**, 83–89 (2024). https://doi.org/10.62476/apr62.83
19. L. K. Abdullayeva and M. H. Hasanov, New Mater., Compd. Appl. **8**, 135–141(2024). https://doi.org/10.62476/nmca8135
20. A. F. Noori, A. M. Ghaleb, and A. I. Salih, Adv. Phys. Res. **6**, 225–238 (2024). https://doi.org/10.62476/apr63225
21. A. F. Gochuyeva, A. M. Mehdiyeva, and S. V. Bakhshaliyeva, New Mater. Compd. Appl. **8**, 87 (2024). https://doi.org/10.62476/nmca8187
22. C. J. Neufeld, S. C. Cruz, R. M. Farrell, et al., Appl. Phys. Lett. **98**, 243507 (2011). https://doi.org/10.1063/1.3595487
23. K. V. Zolotarev, A. N. Mikhailov, V. I. Nakhod, et al., New Mater. Compd. Appl. **8**, 162 (2024). https://doi.org/10.62476/nmca82162
24. K. X. Wang, Z. Yu, V. Liu, et al., Nano Lett. **12**, 1616 (2012). https://doi.org/10.1021/nl204550q
25. X. Meng, E. Drouard, G. Gomard, et al., Opt. Express **20**, A560 (2012). https://doi.org/10.1364/OE.20.00A560
26. A. Abass, K. Q. Le, A. Alù, et al., Phys. Rev. B **85**, 115449 (2012). https://doi.org/10.1103/PhysRevB.85.115449
27. R. Chriki, A. Yanai, J. Shappir, et al., Opt. Express **21**, A382 (2013). https://doi.org/10.1364/OE.21.00A382
28. W. C. Hsu, J. K. Tong, M. S. Branham, et al., Opt. Commun. **377**, 52 (2016). https://doi.org/10.1016/j.optcom.2016.04.055
29. O. Isabella, R. Vismara, A. Ingenito, et al., Opt. Express **24**, A708 (2016). https://doi.org/10.1364/OE.24.00A708
30. K. Kourchid, R. Alaya, N. Bouguila, et al., Russ. J. Phys. Chem. B **18**, 37 (2024). https://doi.org/10.1134/S1990793124010317
31. M. Monajjemi, F. Mollaamin, S. Shahriari, et al., Russ. J. Phys. Chem. B **18**, 1217 (2024). https://doi.org/10.1134/S1990793124700349
32. I. Asfour, Russ. J. Phys. Chem. B **18**, 83 (2024). https://doi.org/10.1134/S1990793124010032
33. Y.-C. Pu, M. G. Kibria, Z. Mi, et al., J. Phys. Chem. Lett. **6**, 2649 (2015). https://doi.org/10.1021/acs.jpclett.5b00909
34. M. L. Reed, E. A. Berkman, M. J. Reed, et al., MRS Online Proc. Libr. **798**, 742 (2003). https://doi.org/10.1557/PROC-798-Y8.6
35. W. Zhang, R. Deng, M. Luo, et al., AIP Adv. **14**, 045301 (2024). https://doi.org/10.1063/5.0202164
36. J. Lin, Y. Yu, Z. Xu, et al., J. Power Sources **450**, 227578 (2020). https://doi.org/10.1016/j.jpowsour.2019.227578
37. M. I. Ikim, E. Y. Spiridonova, V. F. Gromov, et al., Russ. J. Phys. Chem. B **18**, 283 (2024). https://doi.org/10.1134/S199079312401010X
38. M. I. Ikim, E. Y. Spiridonova, V. F. Gromov, et al., Russ. J. Phys. Chem. B **17**, 774 (2023). https://doi.org/10.1134/S199079312303003X
39. U. K. Kumawat, K. Kumar, P. Bhardwaj, et al., Energy Sci. Eng. **7**, 2469 (2019). https://doi.org/10.1002/ese3.436
40. F. Mollaamin and M. Monajjemi, Russ. J. Phys. Chem. B **18**, 49 (2024). https://doi.org/10.1134/S1990793124010159
41. B. Khalili Hadad, F. Mollaamin, and M. Monajjemi, Russ. Chem. Bull. **60**, 238 (2011). https://doi.org/10.1007/s11172-011-0039-5
42. F. Mollaamin and M. Monajjemi, J. Cluster Sci. **34**, 2901 (2023). https://doi.org/10.1007/s10876-023-02436-5
43. M. Monajjemi, F. Mollaamin, and S. Shojaei, Biointerface Res. Appl. Chem. **10**, 5575 (2020). https://doi.org/10.33263/BRIAC103.575585
44. F. Mollaamin, S. Shahriari, M. Monajjemi, et al., J. Cluster Sci. **34**, 1547 (2023). https://doi.org/10.1007/s10876-022-02335-1
45. M. Monajjemi, S. Mohammadi, S. Shahriari, et al., Russ. J. Phys. Chem. B **18**, 308 (2024). https://doi.org/10.1134/S1990793124010342

46. F. Mollaamin and M. Monajjemi, J. Mol. Model. **29**, 170 (2023). https://doi.org/10.1007/s00894-023-05567-8

47. F. Mollaamin, S. Mohammadi, Z. Khalaj, et al., Russ. J. Phys. Chem. B **18**, 67 (2024). https://doi.org/10.1134/S1990793124010330

48. M. Monajjemi and F. Mollaamin, Energies **17**, 4530 (2024). https://doi.org/10.3390/en17184530

49. F. Mollaamin and M. Monajjemi, Sensor Rev. **43**, 266 (2023). https://doi.org/10.1108/SR-03-2023-0040

50. F. Mollaamin and M. Monajjemi, C.-J. Carbon Res. **9**, 20 (2023). https://doi.org/10.3390/c9010020

51. S. H. Vosko, L. Wilk, and M. Nusair, Can. J. Phys. **58**, 1200 (1980). https://doi.org/10.1139/p80-159

52. F. Mollaamin and M. Monajjemi, Int. J. Quantum Chem. **124**, e27348 (2024). https://doi.org/10.1002/qua.27348

53. F. Mollaamin and M. Monajjemi, Mol. Simul. **49**, 365 (2023). https://doi.org/10.1080/08927022.2022.2159996

54. M. J. Frisch, G. W. Trucks, H. B. Schlegel, G. E. Scuseria, M. A. Robb, J. R. Cheeseman, G. Scalmani, V. Barone, G. A. Petersson, H. Nakatsuji, X. Li, M. Caricato, A. V. Marenich, J. Bloino, B. G. Janesko, R. Gomperts, B. Mennucci, H. P. Hratchian, J. V. Ortiz, A. F. Izmaylov, J. L. Sonnenberg, D. Williams-Young, F. Ding, F. Lipparini, F. Egidi, J. Goings, B. Peng, A. Petrone, T. Henderson, D. Ranasinghe, V. G. Zakrzewski, J. Gao, N. Rega, G. Zheng, W. Liang, M. Hada, M. Ehara, K. Toyota, R. Fukuda, J. Hasegawa, M. Ishida, T. Nakajima, Y. Honda, O. Kitao, H. Nakai, T. Vreven, K. Throssell, J. A. Montgomery, Jr., J. E. Peralta, F. Ogliaro, M. J. Bearpark, J. J. Heyd, E. N. Brothers, K. N. Kudin, V. N. Staroverov, T. A. Keith, R. Kobayashi, J. Normand, K. Raghavachari, A. P. Rendell, J. C. Burant, S. S. Iyengar, J. Tomasi, M. Cossi, J. M. Millam, M. Klene, C. Adamo, R. Cammi, J. W. Ochterski, R. L. Martin, K. Morokuma, O. Farkas, J. B. Foresman, and D. J. Fox, *Gaussian 16, Revision C.01* (Gaussian, Inc., Wallingford, CT, 2016).

55. R. Dennington, T. A. Keith, and J. M. Millam, *GaussView, Version 6.06.16* (Semichem Inc., Shawnee Mission, KS, 2016).

56. F. Mollaamin and M. Monajjemi, Comput. Theor. Chem. **1237**, 114646 (2024). https://doi.org/10.1016/j.comptc.2024.114646

57. R. Sciotto, I. A. Ruiz Alvarado, and W. G. Schmidt, Surfaces **7**, 79 (2024). https://doi.org/10.3390/surfaces7010006

58. J. Luo, C. Wang, Z. Wang, et al., Chin. Phys. B **29**, 067402 (2020). https://doi.org/10.1088/1674-1056/ab892d

59. F. Mollaamin and M. Monajjemi, J. Mol. Struct. **1300**, 137214 (2024). https://doi.org/10.1016/j.molstruc.2023.137214

60. E. V. Morozov, A. V. Il'ichev, and V. M. Bouznik, Russ. J. Phys. Chem. B **17**, 1361 (2023). https://doi.org/10.1134/S1990793123060064

61. M. A. A. Zadeh, H. Lari, L. Kharghanian, et al., J. Comput. Theor. Nanosci. **12**, 4358 (2015). https://doi.org/10.1166/jctn.2015.4366

62. M. Monajjemi, S. Afsharnezhad, M. R. Jaafari, et al., Chemistry **17**, 55 (2008).

63. K. Bakhshi, F. Mollaamin, and M. Monajjemi, J. Comput. Theor. Nanosci. **8**, 763 (2011). https://doi.org/10.1166/jctn.2011.1750

64. M. Monajjemi, A. Sobhanmanesh, and F. Mollaamin, Fulleren Nanotubes Carbon Nanostruct. **21**, 47 (2013). https://doi.org/10.1080/1536383X.2011.574325

65. F. Mollaamin and M. Monajjemi, J. Mol. Model. **29**, 119 (2023). https://doi.org/10.1007/s00894-023-05526-3

66. F. Mollaamin and M. Monajjemi, Comput. Theor. Chem. **1237**, 114666 (2024). https://doi.org/10.1016/j.comptc.2024.114666

67. V. Y. Agroskin, B. G. Bravy, G. K. Vasiliev, et al., Russ. J. Phys. Chem. B **17**, 1265 (2023). https://doi.org/10.1134/S1990793123060131

68. L. I. Trakhtenberg, Russ. J. Phys. Chem. B **17**, 600 (2023). https://doi.org/10.1134/S1990793123030144

69. V. A. Aleksandrova and A. M. Futoryanskaya, Russ. J. Phys. Chem. B **17**, 1394 (2023). https://doi.org/10.1134/S1990793123060143

70. Z. Xu, C. Qin, Y. Yu, et al., AIP Adv. **14**, 055114 (2024). https://doi.org/10.1063/5.0208082

71. N. M. O'Boyle, A. L. Tenderholt, and K. M. Langner, J. Comput. Chem. **29**, 839 (2008). https://doi.org/10.1002/jcc.20823

72. A. D. Becke and K. E. Edgecombe, J. Chem. Phys. **9**, 5397 (1990). https://doi.org/10.1063/1.458517

73. S. N. Steinmann, Y. Mob, C. Corminboeuf, Phys. Chem. Chem. Phys. **13**, 20584 (2011). https://doi.org/10.1039/C1CP21055F

74. L. Tian, C. Feiwu, W. Xuebao, Acta Phys. Chim. Sin. **27**, 2786 (2011). https://doi.org/10.3866/PKU.WHXB20112786

75. F. Mollaamin and M. Monajjemi, Russ. J. Phys. Chem. B **17**, 658 (2023). https://doi.org/10.1134/S1990793123030223

76. A. Savin, O. Jepsen, J. Flad, et al., Angew. Chem. Int. Ed. Engl. **31**, 187 (1992). https://doi.org/10.1002/anie.199201871

77. F. Mollaamin, J. Comput. Theor. Nanosci. **11**, 2393 (2014). https://doi.org/10.1166/jctn.2014.3653

78. M. Monajjemi, H. Yamola, and F. Mollaamin, Fulleren Nanotubes Carbon Nanostruct. **22**, 595 (2014). https://doi.org/10.1080/1536383X.2012.702163

79. F. Mollaamin, F. Najafi, M. Khaleghian, B. Khalili Hadad, and M. Monajjemi, Fulleren Nanotubes Carbon Nanostruct. **19**, 653 (2011). https://doi.org/10.1080/1536383X.2010.504956

80. S. Shahriari, F. Mollaamin, and M. Monajjemi, Micromachines **14**, 241 (2023). https://doi.org/10.3390/mi14020241

81. F. Mollaamin and M. Monajjemi, J. Bio- Tribo-Corros. **9**, 33 (2023). https://doi.org/10.1007/s40735-023-00751-y

82. F. Mollaamin, Russ. J. Phys. Chem. B **18**, 805 (2024). https://doi.org/10.1134/S1990793124700131

83. V. V. Parakhin, V. M. Volokhov, E. S. Amosova, et al., Russ. J. Phys. Chem. B **18**, 697 (2024). https://doi.org/10.1134/S1990793124700088

84. F. Mollaamin, S. Shahriari, and M. Monajjemi, Russ. J. Phys. Chem. B **18**, 398 (2024). https://doi.org/10.1134/S199079312402026X

85. F. Mollaamin and M. Monajjemi, Russ. J. Phys. Chem. B **18**, 607 (2024). https://doi.org/10.1134/S1990793124020271

86. E. F. Nemova, T. V. Kobzeva, and G. G. Dultseva, Russ. J. Phys. Chem. B **18**, 95 (2024). https://doi.org/10.1134/S1990793124010354